



HAL
open science

On the Inelastic Mechanical Behavior of Granite: Study Based on Quasi-oedometric and Indentation Tests

H. Shariati, M. Saadati, A. Bouterf, K. Weddfelt, P.L. Larsson, François Hild

► **To cite this version:**

H. Shariati, M. Saadati, A. Bouterf, K. Weddfelt, P.L. Larsson, et al.. On the Inelastic Mechanical Behavior of Granite: Study Based on Quasi-oedometric and Indentation Tests. *Rock Mechanics and Rock Engineering*, 2019, 52, pp.645-657. 10.1007/s00603-018-1646-3 . hal-01924594

HAL Id: hal-01924594

<https://hal.science/hal-01924594v1>

Submitted on 16 Nov 2018

HAL is a multi-disciplinary open access archive for the deposit and dissemination of scientific research documents, whether they are published or not. The documents may come from teaching and research institutions in France or abroad, or from public or private research centers.

L'archive ouverte pluridisciplinaire **HAL**, est destinée au dépôt et à la diffusion de documents scientifiques de niveau recherche, publiés ou non, émanant des établissements d'enseignement et de recherche français ou étrangers, des laboratoires publics ou privés.

On the inelastic mechanical behavior of granite: Study based on quasi-oedometric and indentation tests

H. Shariati ^a, M. Saadati ^{a,b,*}, A. Bouterf ^c, K. Weddfelt ^b, P.-L. Larsson ^a, F. Hild ^c

^a *Department of Solid Mechanics, KTH Royal Institute of Technology, Stockholm, Sweden*

^b *Atlas Copco, Örebro, Sweden*

^c *Laboratoire de Mécanique et Technologie (LMT), ENS Paris-Saclay, CNRS, Université Paris-Saclay, Cachan, France*

Abstract

The inelastic behavior of Bohus granite is investigated based on experimental and numerical results. The yield surface and related dilation angle are determined based on quasi-oedometric tests performed in an earlier work. It is shown how to obtain the yield surface and dilation angle from this test for hydrostatic pressure levels up to 750 MPa. In the constitutive modeling, a Drucker-Prager law is employed together with a variable dilation angle. The constitutive model is first applied to simulate the quasi-oedometric test and the stress and strain fields are obtained. Furthermore, the validation of the model is investigated by simulation of the spherical indentation test. The results are compared with corresponding experimental data and a good agreement is found.

Keywords: Quasi-static indentation, granite, inelastic behavior, tomography

1 Introduction

The fragmentation response of quasi-brittle materials subjected to quasi-static (Q-S) or dynamic loadings has been widely studied in the literature (Price and Farmer 1979; Cook et al. 1984; Vermeer and De Borst 1984; Detournay 1986; Pang and Goldsmith 1990; Liu et al. 2002; Saksala 2011, 2013; Zhao and Cai 2010; Saksala 2010; Wang et al. 2011; Arzúa and Alejano 2013; Saadati et al. 2014, 2016, 2018; Tkalich et al. 2016; Weddfelt et al. 2017). Cook et al. (Cook et al. 1984) investigated the fracture process by performing Q-S indentation tests on rock samples using circular flat-bottomed indenters with different sizes. The authors described

* Corresponding author: Department of Solid Mechanics, KTH Royal Institute of Technology, Stockholm, Sweden.
Email address: msaadati@kth.se (M. Saadati).

different stages of fragmentation based on the recorded force penetration response. The formation of a crater, a crushed zone and a region with multiple cracks were studied. In another study (Liu et al. 2002), a numerical method was developed in order to analyze the interaction between rock and tool. The rock was loaded by single and double indenters and the fragmentation process was simulated. Wang et al. (Wang et al. 2011) utilized a numerical tool to simulate indented rock fragmentation in which heterogeneity and isotropic damage were taken into consideration. In the work of Saksala (Saksala 2010), a damage-viscoplastic cap constitutive model was considered when simulating a rock sample behavior under low-velocity impact. A phenomenological and isotropic damage model in tension was combined with a viscoplastic model and cap in compression. The constitutive model was used to numerically investigate the interaction between drill bits and rock under axisymmetric conditions (Saksala 2011) and later it was also extended to a 3D case (Saksala 2013).

The fragmentation response of Bohus granite was investigated by some of the present authors (Saadati et al. 2014, 2018). A combination of pressure dependent plasticity (i.e. Krieg, Swenson and Taylor (KST) model) and an anisotropic damage model (proposed by Denoual, Forquin and Hild (DFH) model) was adopted to explain its response (Saadati et al. 2014). The results were validated based on a series of experiments. In that work, the size and rate effects on the tensile strength of a semi-brittle material such as Bohus granite were assumed to interact with each other. This interaction was explained within the framework of a Weibull model (Weibull 1939, 1951) and based on a random distribution of initial defects with different sizes in the material (Jayatilaka and Trustrum 1977). The rate effect on the tensile strength of Bohus granite was investigated using Hopkinson bar experiments and spalling tests. It was shown that the tensile strength increased from 8 MPa under Q-S conditions to 19 MPa in the dynamic case (Saadati et al. 2016). Further, the size effect on the tensile strength of Bohus granite was investigated by performing three-point bend tests on specimens of different sizes and using the Weibull size effect and the concept of effective volume (Weibull 1952; Davies 1973; Hild and Marquis 1992), namely, the portion of the total volume that is subjected to a positive equivalent stress (Saadati et al. 2018). Furthermore in indentation applications the effective volume was calculated for a semi-infinite medium loaded by a cylindrical indenter and using a probabilistic approach (Weddfelt et al. 2017). In percussive drilling, both rate and size effects on the tensile strength play an important role in the fragmentation response and the combination of them is needed to explain these phenomena. However, considering the small values of the effective volume during indentation testing (Weddfelt et al. 2017), the rate dependence of Bohus granite

based on previous studies performed by the authors and also the range of strain rates occurring in percussive drilling (Saadati et al. 2016), the rate effect should be less critical than the size effect (Weddfelt et al. 2017). It should also be mentioned that any size effect in the compressive behavior was excluded in that study.

In the present work, the inelastic constitutive behavior of the material is investigated based on, in particular, quasi-oedometric compression tests performed in an earlier work (Saadati et al. 2018). The results from those tests are used herein to obtain the dilation angle for hydrostatic pressure levels up to 750 MPa. From these experimental results, together with corresponding finite element simulations of the same test, it is suggested that a linear Drucker-Prager law, with a variable dilation angle, can be used to model the inelastic behavior of granite. One of the other interests of the present work is to investigate the Q-S force-penetration ($P-h$) response of Bohus granite loaded by a spherical indenter, and thereby also validating the employed material model. The attention is primarily put on the loading range up to the first main load drop, corresponding to the load capacity of the material (Weddfelt et al. 2017), in order to avoid effects due to cracking in the constitutive modelling.

A number of Q-S indentation tests was carried out in the present work and the corresponding $P-h$ response of Bohus granite was obtained. The generated experimental data are then compared to the results produced by numerical finite element simulations taking advantage of the Abaqus FE software (Abaqus 2014). Additionally, a high speed camera was utilized in order to study the upper surface of the specimen during the indentation test. A series of images from the sample surface was captured right before and after the load-drops in the force penetration response of the studied rock. Furthermore, the tested specimens were scanned by x-ray microtomography with the intent of better understanding the cracking mechanism. It should be mentioned that Bohus granite, which is selected for experimental purposes, mainly contains quartz (33 vol%), plagioclase (33 vol%), potassium feldspar (29 vol%) and biotite (6 vol%), which was tested by SP, Swedish National Testing and Research Institute (Saadati 2015).

A review of the literature reveals that the dilation angle is one of the critical material parameters that should be carefully treated since the evaluation of the inelastic behavior is significantly influenced by it (Vermeer and De Borst 1984). It is, in some cases either neglected, i.e. referred to as incompressible flow rule (Yu 2000), or set equal to the friction angle for which an associated flow rule (Bland 1957) is considered. Neither of these two

assumptions are necessarily representative of the inelastic behavior of rocks (Price and Farmer 1979; Vermeer and De Borst 1984). Due to practical difficulties in measuring such a parameter, especially at high levels of hydrostatic pressure, the approximation of a constant dilation angle is usually made (Saksala 2010). The dilation angle, however, is known to change as a function of the inelastic strain level (Detournay 1986; Zhao and Cai 2010; Arzúa and Alejano 2013; Tkalich et al. 2016). It should be mentioned that it is not straightforward to obtain the dilation angle experimentally at high levels of hydrostatic pressure. For instance, triaxial tests were used and experimental results for the dilation angle were obtained for hydrostatic pressures up to 200 MPa and assumptions were made for higher levels (Tkalich et al. 2016). For indentation applications, much higher pressure levels are expected (Saadati et al. 2014).

2 Experiments

In this section, the experimental part of the present analysis is described. These tests were conducted in order to investigate the inelastic behavior of the material and to validate the employed material model in a situation similar to what could be expected in indentation.

2.1 *Quasi-oedometric compression test*

The inelastic behavior of the material is investigated based on quasi-oedometric compression tests performed in an earlier work (Saadati et al. 2018) with the intention of determining the yield surface and dilation angle. During the quasi-oedometric test, a cylindrical specimen enclosed within a confinement cell was axially loaded in compression (see Figure 1). Both axial and radial stresses increase during loading as the material expands in the lateral direction. This gives an indication of the strength of the material at different levels of hydrostatic pressure. Stress-strain curves, deviatoric and volumetric responses of the rock material were recorded at different hydrostatic pressure levels. Granite cylinders 28.9 mm in diameter and 40 mm in length were loaded at a strain rate of 10^{-3} 1/s and the maximum load (1100 kN) of the machine reached during the test. The results from those tests are used hereafter to obtain the dilation angle for hydrostatic pressure levels up to 750 MPa.

2.2 *Quasi-static indentation*

Quasi-static indentation tests, schematically shown in Figure 2, were performed on Bohus granite in order to investigate its mechanical behavior with in particular the cracking behavior. Rock blocks $15 \times 15 \times 15$ cm³ in size were indented by means of a tungsten carbide spherical indenter 12 mm in diameter ($R = 6$ mm). The size of the rock block ensures that boundary

effects on relevant indentation quantities are negligible. The tungsten carbide elastic modulus is almost ten times larger than that of granite (52 GPa) and for this reason the indenter will be considered as rigid in the numerical simulations. This rigidity assumption was also employed elsewhere (Shaoquan 1995). Quasi-static (Q-S) tests were carried out using a 100 kN servo-controlled testing machine. A manufactured cylinder was utilized in order to press the indenter onto the rock surface, see Figure 3(b). Two linear variable displacement transducers (LVDTs) were secured in the manufactured holder by means of two screws (Figure 3(a)). The penetration depth was measured by means of LVDTs. The tests were conducted in displacement control mode at a constant velocity of 5 $\mu\text{m/s}$. The response from the load cell of the testing machine was recorded, which is used later on to validate the numerical model.

Figure 4 shows the force-penetration ($P-h$) response of Bohus granite during four Q-S indentation tests that were carried out in the present work. The force versus penetration response is almost linear with an initial small non-linearity. This linearity, which is a result of the inelastic material behavior, suggests in the case of spherical indentation that strain hardening is small or negligible (Storåkers et al. 1997). Small load-drops in the force signal are observed before the load capacity of the material is reached. These small load-drops are mainly due to conical, Hertzian cracks initiated immediately outside the contact area to be discussed in more detail below. The $P-h$ response shows a large load-drop for applied load levels ranging from 35 to 42 kN corresponding to indentation (penetration) depths of about 0.5 mm. Prior to these large load-drops, the response of the material is very reproducible, which indicates that the effect of the material heterogeneities is negligible at this scale of observation.

In order to investigate the reason behind the detected load-drops in the experimental $P-h$ response, a high speed camera was utilized to capture images of the rock specimen surface before and after the load-drops. Figure 5(a) shows the force versus axial displacement curve of Experiment 5. This displacement is that of the actuator of the testing machine. It should be noted that the displacement from the actuator should be corrected for the machine compliance to be consistent with the penetration depth from LVDTs in the other tests. LVDTs were not utilized during this experiment, since images of the rock surface close to the indentation zone were acquired. The images were captured for one of the small load-drops and the large load-drop, which are shown with the first red circle and the second blue circle in Figure 5(a), respectively. These images are shown in Figure 5(b)-(e). Several experiments were performed and it was noticed that each load-drop corresponded to material removal on the block surface. These observations suggest that the large load-drop in the $P-h$ response was mainly due to

chipping caused by lateral expansion of the inelastically deformed material under the indenter (Shaoquan 1995) and that the small load drops are due to ring (Hertzian) cracking immediately outside the contact boundary. The absence of substantial sub-surface cracking will be checked by Computed Tomography (CT) observations discussed below.

2.3 *Computed Tomography (CT) observations*

The tested specimens were scanned in a North Star Imaging X50+ tomograph. The acquisition parameters were 90KV-voltage, 220 μ A-intensity, 1944 \times 1536-pixel flat panel definition. The physical size of one voxel was 25.4 μ m. One thousand and two hundred radiographs were acquired over 360° rotation of the tomographic stage. The total acquisition time was one hour and a half. A filtered back-projection algorithm enabled 3D volumes to be reconstructed. The CT images are presented in Figure 6, showing a large part of the indented material with the extent of the contact surface indicated.

There are no visible sub-surface cracks in Figure 6. As mentioned above, it cannot be ruled out that some small sub-surface median cracks were formed during the initial loading stages partially causing some of the small load-drops. As seen in Figure 6, they were trapped in the material, with its specific grain formation, by the crushed zone and were not formed at higher load levels. Therefore the effect of such damage on the $P-h$ response of Bohus granite during Q-S indentation tests up to the load capacity of the material is assumed to be negligible. An elastoplastic model can be employed and determined in the absence of any damage influencing the inelastic behavior.

It should be emphasized that the term damage corresponds to tensile failure (i.e. mode I fracture) within the context of this work. Any other form of inelastic deformation discussed hereafter, due to shear or compaction, is considered as plasticity.

Furthermore in Figure 6, surface cracking in the form of chipping is seen and, together with the observations from the high speed camera images, it can be stated that this surface cracking is the reason for the large load-drops. The chipping initiates approximately at the contact boundary due to high tensile surface stresses as discussed in more detail below where stress distributions from finite element simulations will be presented. In the images of Figure 6 there are also indications of small side cracks just below the specimen surface outside the contact boundary. Most often, such side cracks were formed during unloading (Yu 2000) and are indeed predicted by the finite element simulations, see below.

2.4 Summary of the experimental results

The results from quasi-oedometric compression tests performed in an earlier work (Saadati et al. 2018) will be used to investigate the inelastic behavior of the material and to obtain the yield surface and dilation angle for hydrostatic pressure levels up to 750 MPa.

The experimental results from the indentation tests, utilizing high speed cameras and Computed Tomography, made it possible to draw the following conclusions:

- Sub-surface cracking is negligible at levels up to the load capacity of the material.
- The large drop at the load capacity is due to chipping close to the specimen surface caused by high tensile surface stresses at the contact boundary.
- The repeated small load-drops during loading are due to ring (Hertzian) cracking immediately outside the contact boundary. These cracks have a negligible influence on the $P-h$ response.

From the experimental part of the present investigation, it is concluded that cracking has a limited influence on the macroscopic indentation behavior up to the first major load-drop.

3 Inelastic constitutive modeling

The fragmentation response of Bohus granite in percussive drilling has been investigated in the literature. A combination of parabolic pressure-dependent plasticity (KST) and anisotropic damage model (DFH) was adopted to explain its response (Saadati et al. 2014). It was concluded that the fragmentation response was mainly due to the tensile strength and therefore a relatively simple plasticity model for the compressive behavior was coupled to a comprehensive damage model (Denoual and Hild 2000; Forquin and Hild 2010) for the tensile part to explain the fragmentation process. In the present work, the Q-S force-penetration response of Bohus granite loaded by a spherical indenter up to the first main load-drop (defining the load capacity of the material) is of primary interest.

As the compressive behavior under the indenter and accordingly the plasticity model plays a critical role in the $P-h$ response, special attention is paid to implement such a model, which is calibrated with the quasi-oedometric compression test performed in an earlier work (Saadati et al. 2018). The yield surface and dilation angle are obtained from this test up to a hydrostatic pressure level of about 750 MPa. The yield surface has an almost linear shape up to this pressure level and therefore a simple linear Drucker-Prager (D-P) model seems sufficient for

the yield surface. However, unlike the KST model that neglects the inelastic volumetric change due to shear, the dilation angle obtained from the quasi-oedometric test is added to the plasticity model. On the other hand, the damage effect on the P - h response up to the first main load drop is assumed to be minor as neither ring cracks nor the possible trapped median cracks have significant effects on the stiffness of the material. Therefore, only the plasticity model is employed in the absence of any damage description and observation (see Section 2). This assumption, however, will be qualitatively and quantitatively validated in the remainder of the paper. The methodology in the present study is different from that of (Saadati et al. 2014) in which the fragmentation mechanism and accordingly the damage behavior were of primary interest, and the indentation was not necessarily limited up to the first main load drop.

The inelastic constitutive modelling will be described as follows. In Section 3.1, the basis for the linear D-P-model will be presented. In Section 3.2, the corresponding material parameters for such a model are determined from previous experimental results (Saadati et al. 2018). Then in Section 3.3, the constitutive model is first applied to simulate the quasi-oedometric test and the stress and strain fields are compared with corresponding experimental data (Saadati et al. 2018). Then a validation of the model will be performed based on the quasi-static indentation results.

3.1 *Elasto-plastic model*

Geological materials such as rocks exhibit pressure-dependent yield behavior in which they yield at higher load levels as the pressure increases (Saadati et al. 2014). Therefore, partly due to simplicity, but mainly based on present and previous experimental findings, a linear D-P model (Drucker and Prager 1952) is employed in order to numerically simulate the quasi-static indentation tests reported herein, see Figure 7. It should be mentioned that nonlinear yield surfaces or damage can be incorporated in the model but are deemed unnecessary (Saadati et al. 2018). The selected model includes inelastic dilation, which is the volume change when the material is subjected to shear strains, and inelastic shearing. The linear Drucker-Prager criterion is written as

$$F = q - p \tan \beta - d = 0 \quad (1)$$

where F is yield function, d the cohesion of the material, β the friction angle, q von Mises equivalent stress

$$q = \sqrt{\frac{3}{2}(\mathbf{S}:\mathbf{S})} \quad (2)$$

\mathbf{S} the stress deviator,

$$\mathbf{S} = \boldsymbol{\sigma} + p\mathbf{I} \quad (3)$$

$\boldsymbol{\sigma}$ the stress tensor, and p the pressure

$$p = -\frac{1}{3}\text{trace}(\boldsymbol{\sigma}) \quad (4)$$

As for inelastic yielding, the flow potential (G) reads

$$G = q - p \tan \Psi \quad (5)$$

where Ψ is the dilation angle, which is shown schematically in Figure 7(a). If $\Psi = 0$, the material is incompressible (i.e., the inelastic strain tensor is deviatoric), and when $\Psi > 0$ the material dilates with the applied pressure. For materials such as rocks, the linear D-P model is normally employed with non-associated flow rule (Tkalich et al. 2016), which means that the inelastic flow is assumed to be at angle Ψ with respect to the q -axis in the q - p plane, and $\Psi \neq \beta$ (Figure 7). It should be noted that associated flow rule implies that $\Psi = \beta$. The inelastic strain increment is expressed as

$$d\boldsymbol{\varepsilon}^i = d\lambda \frac{\partial G}{\partial \boldsymbol{\sigma}} \quad (6)$$

where $d\lambda$ is the inelastic strain rate multiplier, and $\boldsymbol{\varepsilon}^i$ the inelastic strain tensor. As mentioned in Section 2.2, the linearity in the experimental P - h response suggests that strain hardening is negligible, and therefore an ideal inelastic (plastic) behavior is assumed in the numerical simulations below.

3.2 Material parameters

An experimentally determined set of parameters is presented in this section. The D-P model parameters for Bohus granite, which are summarized in Table 1, are the same as in the KST model determined in a previous experimental work (Saadati et al. 2018). The elastic modulus (E) and Poisson's ratio (ν) were determined from uniaxial tensile and compressive tests. The Poisson's ratio value was initially 0.15 (Saadati et al. 2018) because of pre-existing structural cracks in some of the specimens, and later during loading became equal to 0.25 due to closure

of those cracks. In this study, the Poisson's ratio is assumed equal to 0.25, which corresponds to an intact specimen.

The dilation angle (Ψ), which corresponds to the volume change when the material is subjected to shear strains, is derived from Equation (6) and formulated as

$$\Psi = \tan^{-1} \left(\frac{3}{3 \frac{\dot{\varepsilon}_a^i}{\dot{\varepsilon}_v^i} - 1} \right) \quad (7)$$

where $\dot{\varepsilon}_a^i$ is the inelastic axial strain rate, and $\dot{\varepsilon}_v^i$ the inelastic volumetric strain rate. As seen from this equation, the dilation angle is only a function of the ratio between the inelastic axial and volumetric strain rates. This ratio is also determined from the previously mentioned quasi-oedometric compression test results (Saadati et al. 2018). The inelastic axial strain increment is plotted against the inelastic volumetric strain increment in Figure 8(a) for the considered quasi-oedometric test (Saadati et al. 2018). A piecewise linear approximation function is fitted to the test results. This piecewise function is composed of successive lines whose slopes are calculated and used to determine the dilation angles. In fact, the dilation angle is approximated as a function of the inelastic volumetric strain that is by itself related to the pressure. Consequently, the dilation angle can be set dependent on pressure in the constitutive model. Additionally the dilation angle is plotted against the pressure level in Figure 8(b). The experimentally determined dilation angle is initially equal to 61° and decreases to 0° at the end of the quasi-oedometric experiment corresponding to approximately 750 MPa pressure.

Since the quasi-oedometric results show an almost linear yield surface at relatively high pressure levels, a simple linear D-P model with constant friction angle is used for numerical modeling purposes. It should be mentioned that the dilation angle should not exceed the friction angle, i.e. $\Psi \leq \beta$, in order to be thermodynamically consistent (Saksala 2010). Consequently, any values of experimentally determined dilation angle that are greater than the friction angle in constitutive modeling are set equal to the friction angle in order to be thermodynamically consistent.

3.3 Analysis of the quasi-oedometric test

A finite element simulation (based on the hypotheses discussed in Sections 3.1 and 3.2) of the quasi-oedometric test is performed using Abaqus software (Abaqus 2014) and the results are

compared with corresponding experimental data (Saadati et al. 2018). The test setup and geometry of the rock sample is defined according to Section 2.1 (see Figure 1). The steel parts are assumed to be linearly elastic with Young's modulus being 205 GPa, and Poisson's ratio equal to 0.29. An axisymmetric model of the quasi-oedometric test using 30,000 4-noded elements is used and the axial loading is applied on the rock surface. The contact between the rock sample and the confining cell is assumed to be frictionless.

The comparison between the present finite element results and experimental data (Saadati et al. 2018) is detailed in Figure 9. In Figure 9(a) the predicted yield surfaces are compared, and correspondingly for inelastic axial strain field in Figure 9(b). The agreement between the two sets of results is good, which gives confidence in the presently used model for the inelastic behavior of granite.

As observed in the experimental results, the material behaves linearly up to a hydrostatic pressure of about 300 MPa when it is loaded in a quasi-oedometric test (Figure 9(a)). Therefore this test is suitable to give inelastic data for higher levels of hydrostatic pressure, which is the case in indentation.

The total axial strain in the rock sample was measured during the experiments using LVDTs and the radial strain was calculated based on the strain gauge data glued on the outer surface of the confining cell (Saadati et al. 2018). The total strain in the rock is divided into elastic and inelastic parts, in which the elastic part is calculated using linear elasticity with Young's modulus being 52 GPa, and Poisson's ratio equal to 0.25.

As seen in Figure 9(b), the initial difference between the experimental and simulation results for the inelastic axial strain is a consequence of the slight discrepancies in the yield surfaces and corresponds to the fact that inelastic deformations initiate slightly earlier in the test compared with the simulation.

4 Numerical analysis and results of the indentation test

In this section the finite element analysis of the indentation test is detailed and the corresponding results are discussed and compared with the experimental findings. A particular subsection is used to analyze and discuss the influence of the dilation angle Ψ on indentation quantities.

4.1 Finite element analysis

The prediction of the force-penetration response of the indented rock specimen is of particular interest for validation purposes in this study. Various numerical tools are utilized in the literature (Liu et al. 2002; Wang et al. 2011) in order to predict the brittle material response for quasi-static loading and different constitutive models coupled with damage are presented (Saksala 2010; Tkalich et al. 2016). Hardening is considered in some of those studies. However in this investigation, as mentioned above, ideal inelasticity (plasticity) is coupled with a confining pressure dependent dilation angle and was found to be sufficient to capture the linear $P-h$ response.

Abaqus explicit and implicit softwares (Abaqus 2014) will be used for the numerical simulations reported hereafter. By means of symmetries, only one quarter of the problem is modeled in order to reduce the computation time and 8-node linear reduced integration brick elements are used for meshing purposes. The indenter is modeled as a 3D analytical rigid body since its Young's modulus is almost ten times larger than that of rock (this hypothesis reduces the computational cost as well). The load is applied by subjecting the rigid indenter to a vertical displacement. The geometry, mesh and boundary conditions are illustrated in Figure 10. Figure 10(c) shows that the mesh within the indentation zone is denser due to the fact that the stress/strain field gradients are high close to the contact region. An axisymmetric model was also analyzed and the results were identical to the 3D case, which is used for illustrative purposes. It should be mentioned that the 3D geometry is required for simulations utilizing the KST-DFH model to be discussed in more detail below, and therefore most of the simulations were performed using the 3D model. It is worth noting that if additional validations are sought, say via in situ tests, 3D simulations would also be required since symmetric boundary conditions are difficult, if not impossible, to be experimentally prescribed (Bouterf et al. 2014, 2017).

The friction effect is studied by assuming a friction coefficient of 0.5 between the indenter and the rock. It is found that the $P-h$ response up to the first main load drop in the simulation with friction is essentially the same as the $P-h$ response in the simulation without friction. Field variables such as stresses are quantitatively more influenced by frictional effects but this is of less importance as presently such quantities are only of qualitative concern when it comes to the comparisons reported below between experimental and numerical results related to the cracking behavior.

The Young's modulus and Poisson's ratio are defined in the elastic material behavior section in Abaqus and the angle of friction as well as dilation angle are provided in the D-P material behavior section in Abaqus (Abaqus 2014). The dilation angle dependence with the pressure is implemented by using the VUSDFLD user subroutine of Abaqus in order to redefine field variables at each material point. Through Abaqus' input file in the material definition section, the dilation angles are provided at different equivalent pressure (p) levels and linearly interpolated as discussed above.

4.2 Numerical results and comparison with experiments

The resulting force-penetration responses given by the numerical simulations as well as the response from Experiment 1 are plotted in Figure 11 for comparison purposes. The numerical results corresponding to a linear elastic model, the KST (Krieg 1978; Swenson and Taylor 1983) model, the DFH model (Denoual and Hild 2000; Forquin and Hild 2010), and the D-P model with variable dilation angle are compared with experimental results. The numerical results capture Experiment 1 with high accuracy. As also evidenced in Figure 11(a), the slope of the predicted $P-h$ response is almost the same as the experimental $P-h$ curve. Therefore it is argued that the effect of damage is negligible (as confirmed by the reported tomographic observations of Section 2.3).

For completeness, a series of simulations with a D-P model combined with a tension cut off at different hydrostatic stresses, ranging from 10 MPa up to 100 MPa, are also performed. The tension cut-off has an almost negligible effect on the $P-h$ curve as it can be seen in Figure 11(b). However, it should be mentioned that the tension cut off, as a yield criterion, changes the stress state in the pressure region. Since cracking is more of an anisotropic damaging response, with independent stress components, rather than an inelastic constitutive model with yield criterion, it turns out that the tension cut off is not an appropriate choice for the interpretation of the load drops due to cracking.

The pressure (p), the maximum principal and mid principal stress fields at a penetration depth of 0.5 mm, which is followed by the large load-drop in the $P-h$ response of Experiment 1, are shown in Figure 12. Results of the present model (with variable dilation angle) and with zero dilation angle, are reported. The reason behind the formation of a crushed zone under the indenter, which is frequently discussed in the literature (Mishnaevsky Jr 1995; Kalyan et al. 2015), can be understood by looking at Figure 12(b) in which the pressure level is high in the vicinity of the contact zone.

As discussed previously, median sub-surface cracks may possibly initiate during initial loading but are then trapped by the crushed zone due to high pressure levels, see Figure 12(b) and volume expansion due to dilation, which reduce the sub-surface tensile stresses along the symmetry line beneath the indenter. The small load-drops are the result of Hertzian cracking (due to radial stresses) at the continuously growing contact boundary. The crack formation at the first large load-drop is facilitated by the first and second principal stresses at the surface of the rock specimen. These two eigen stresses reach their maximum levels at the indentation (penetration) depth of 0.5 mm corresponding to the first main load drop in the $P-h$ response. The response after this load drop is a combination of major cracking and fragmentation in addition to inelasticity. Therefore further efforts not related to modeling the macroscopic inelastic behavior are needed to simulate such response, which is out of scope of the current work.

Furthermore, some simulations of the unloading stage were also carried through. It is found from these simulations that tensile normal stresses (along the z -axis shown in Figure 2) are created somewhat below the surface during unloading and due to inhomogeneous stress states in the presence of irreversible deformations (Figure 13(a)). These tensile stresses, shown in Figure 13(b), are most likely the reason behind the side crack, which is widely discussed in the literature (Shaoquan 1995) and also present in the reported tomographic observations in Section 2.3.

4.3 Dilation angle influence

As was discussed above, dilation is an important feature when it comes to constitutive modeling of granite. Dilation is the volume change when the material is subjected to shear strains and it was observed in cemented granular materials such as rocks (Vermeer and De Borst 1984). In order to investigate this feature in more details finite element analyses are performed with the intent of examining its influence on the force versus penetration response for spherical indentation. Two different dilation angles are considered assuming no dilation (i.e. $\Psi = 0^\circ$) that enforces incompressible inelasticity, and another one with a high degree of dilation angle (i.e. $\Psi = 50^\circ$). As seen from Figure 14, the forces at penetration depth of 0.5 mm for the simulated problem are equal to 30 and 50 kN for 0° and 50° dilation angles, respectively.

Based on the results of Figure 14 it can first be stated that the $P-h$ response is sensitive to the choice of dilation angle, and secondly, that it would be possible to choose a constant value on the dilation angle and get a good agreement with the experimentally determined $P-h$

response. In the latter case, however, this would not have a solid physical background remembering that the values of Ψ determined from quasi-oedometric tests, see Figure 8, were far from constant and such assumption might lead to a low accuracy of predictions for other types of loading.

Last, it should be mentioned that both KST and D-P models share almost the same yield surface at positive pressures (compression). However, for negative pressures (tension), the yield surface in the D-P model is still valid (up to the tensile strength for the D-P case together with tension cut off), but in the case of the KST model and in the absence of any damage, the yield surface is only defined for positive pressures and the material behaves elastically for negative pressures. This is the reason behind the small difference between the P - h response of KST and D-P (with 0° dilation angle) models.

5 Concluding remarks

The inelastic behavior of granite was investigated based on quasi-oedometric compression tests performed in an earlier work (Saadati et al. 2018) with the intention to determine the yield surface and dilation angle. The results from those tests were used herein to obtain the dilation angle for hydrostatic pressure levels up to 750 MPa. Constitutive modeling of the inelastic (plastic) response of Bohus granite was attempted using a linear Drucker-Prager model with variable dilation angle. A first validation of the constitutive specification was obtained by simulating the quasi-oedometric test using finite element simulations. The results were compared with corresponding experimental data and a good agreement was found. Furthermore, the model was also applied to spherical indentation tests and the P - h response was successfully predicted.

The linear Drucker-Prager model was chosen since it still yielded good agreement between quasi-oedometric test results and the corresponding numerical simulations. The indentation test turned out to be an appropriate choice for the validation of the inelastic response as no major cracking apart from the crushed zone was captured up to the first major load-drop based on high speed imaging and tomographic observations.

Post-mortem tomographic observations showed that damage did develop significantly in the compaction zone while no major crack was observed in other zones. However, this conclusion was drawn based on visual observations only. More thorough quantitative analyses may be considered in the future to assess the damage state via digital volume correlation (Hild

et al. 2015) and in situ tests. Such type of analyses may also allow the proposed model to be probed in a more comprehensive way as was performed for another brittle material (i.e. plaster (Bouterf et al. 2017)).

6 Acknowledgements

The authors would like to thank Dr. Irene Linares Arregui at the Department of Solid Mechanics, KTH for very able experimental assistance and the Odqvist Laboratory for Experimental Mechanics at KTH for providing the high speed camera.

References

- Abaqus (2014) Analysis User's Manual Version 6.14-2. Dassault Syst Simulia Corp Provid RI
- Arzúa J, Alejano LR (2013) Dilation in granite during servo-controlled triaxial strength tests. *Int J Rock Mech Min Sci* 61:43–56
- Bland DR (1957) The associated flow rule of plasticity. *J Mech Phys Solids* 6:71–78
- Bouterf A, Adrien J, Maire E, et al (2017) Identification of the crushing behavior of brittle foam: From indentation to oedometric tests. *J Mech Phys Solids* 98:181–200
- Bouterf A, Roux S, Hild F, et al (2014) Digital Volume Correlation Applied to X-ray Tomography Images from Spherical Indentation Tests on Lightweight Gypsum. *Strain* 50:444–453
- Cook NGW, Hood M, Tsai F (1984) Observations of crack growth in hard rock loaded by an indenter. In: *International Journal of Rock Mechanics and Mining Sciences & Geomechanics Abstracts*. Elsevier, pp 97–107
- Davies DGS (1973) The statistical approach to engineering design in ceramics. In: *Proceedings of the British Ceramic Society*. pp 429–452
- Denoual C, Hild F (2000) A damage model for the dynamic fragmentation of brittle solids. *Comput Methods Appl Mech Eng* 183:247–258
- Detournay E (1986) Elastoplastic model of a deep tunnel for a rock with variable dilatancy. *Rock Mech Rock Eng* 19:99–108
- Drucker DC, Prager W (1952) Soil mechanics and plastic analysis or limit design. *Q Appl Math* 10:157–165
- Forquin P, Hild F (2010) A probabilistic damage model of the dynamic fragmentation process in brittle materials. *Adv Appl Mech* 44:1–72
- Hild F, Bouterf A, Roux S (2015) Damage measurements via DIC. *Int J Fract* 191:77–105
- Hild F, Marquis D (1992) A statistical approach to the rupture of brittle materials. *Eur J Mech Solids* 11:753–765
- Jayatilaka A de S, Trustrum K (1977) Statistical approach to brittle fracture. *J Mater Sci*

12:1426–1430

- Kalyan B, Murthy CSN, Choudhary RP (2015) Rock indentation indices as criteria in rock excavation technology—A critical review. *Procedia Earth Planet Sci* 11:149–158
- Krieg RD (1978) A simple constitutive description for soils and crushable foams. Report, SC-DR-7260883, Sandia Natl Lab
- Liu HY, Kou SQ, Lindqvist P-A, Tang CA (2002) Numerical simulation of the rock fragmentation process induced by indenters. *Int J Rock Mech Min Sci* 39:491–505
- Mishnaevsky Jr LL (1995) Physical mechanisms of hard rock fragmentation under mechanical loading: a review. In: *International journal of rock mechanics and mining sciences & geomechanics abstracts*. Elsevier, pp 763–766
- Pang SS, Goldsmith W (1990) Investigation of crack formation during loading of brittle rock. *Rock Mech Rock Eng* 23:53–63
- Price AM, Farmer IW (1979) Application of yield models to rock. In: *International Journal of Rock Mechanics and Mining Sciences & Geomechanics Abstracts*. Elsevier, pp 157–159
- Saadati M (2015) On the mechanical behavior of granite: Constitutive modeling and application to percussive drilling. KTH Royal Institute of Technology
- Saadati M, Forquin P, Weddfelt K, et al (2018) On the Mechanical Behavior of Granite Material With Particular Emphasis on the Influence From Pre-Existing Cracks and Defects. *J Test Eval* 46:1–13
- Saadati M, Forquin P, Weddfelt K, et al (2014) Granite rock fragmentation at percussive drilling—experimental and numerical investigation. *Int J Numer Anal Methods Geomech* 38:828–843
- Saadati M, Forquin P, Weddfelt K, Larsson PL (2016) On the tensile strength of granite at high strain rates considering the influence from preexisting cracks. *Adv Mater Sci Eng* 2016:. doi: 10.1155/2016/6279571
- Saksala T (2011) Numerical modelling of bit–rock fracture mechanisms in percussive drilling with a continuum approach. *Int J Numer Anal Methods Geomech* 35:1483–1505
- Saksala T (2013) 3D numerical modelling of bit–rock fracture mechanisms in percussive drilling with a multiple-button bit. *Int J Numer Anal methods Geomech* 37:309–324

- Saksala T (2010) Damage–viscoplastic consistency model with a parabolic cap for rocks with brittle and ductile behavior under low-velocity impact loading. *Int J Numer Anal Methods Geomech* 34:1362–1386
- Shaoquan K (1995) Some basic problems in rock breakage by blasting and by indentation
- Storåkers B, Biwa S, Larsson P-L (1997) Similarity analysis of inelastic contact. *Int J Solids Struct* 34:3061–3083
- Swenson D V, Taylor LM (1983) A finite element model for the analysis of tailored pulse stimulation of boreholes. *Int J Numer Anal Methods Geomech* 7:469–484
- Tkalich D, Fourmeau M, Kane A, et al (2016) Experimental and numerical study of Kuru granite under confined compression and indentation. *Int J Rock Mech Min Sci* 87:55–68
- Vermeer PA, De Borst R (1984) Non-associated plasticity for soils, concrete and rock. *HERON*, 29 (3), 1984
- Wang SY, Sloan SW, Liu HY, Tang CA (2011) Numerical simulation of the rock fragmentation process induced by two drill bits subjected to static and dynamic (impact) loading. *Rock Mech Rock Eng* 44:317–332
- Weddfelt K, Saadati M, Larsson P-L (2017) On the load capacity and fracture mechanism of hard rocks at indentation loading. *Int J Rock Mech Min Sci* 100:170–176
- Weibull W (1952) A survey of statistical effects in the field of material failure. *Appl Mech Rev* 5:449–451
- Weibull W (1939) A statistical theory of the strength of materials. *Ingeniors Vetenskaps Akad*
- Weibull W (1951) A Statistical Distribution Function of Wide Applicability. *J Appl Mech* 103:293–297
- Yu H-S (2000) In-Situ Soil Testing. In: *Cavity Expansion Methods in Geomechanics*. Springer, pp 209–274
- Zhao XG, Cai M (2010) A mobilized dilation angle model for rocks. *Int J Rock Mech Min Sci* 47:368–384

Table and table legends

Table 1. Material parameters used in the numerical simulations with the linear Drucker-Prager model.

Material parameter	
E (GPa)	52
ν	0.25
ρ (kg/m ³)	2630
β (°)	51.7
d (MPa)	153.3
Ψ (°)	Figure 8(b)

Figure legends

Figure 1. Experimental quasi-oedometric compression test setup.

Figure 2. Schematic illustration of the spherical indentation test. P is the contact force, h the penetration depth, a the contact radius, and R the spherical indenter radius.

Figure 3. Experimental setup for the spherical indentation test (a) with LVDTs and (b) without LVDTs. The LVDTs are secured in the manufactured holder by means of two screws. The manufactured cylinder is utilized to press the indenter onto the rock surface.

Figure 4. Experimentally determined force-penetration ($P-h$) response of Bohus granite for the spherical indentation tests.

Figure 5. (a) Force-displacement curve corresponding to indentation experiment 5 (in this case axial displacements are reported instead of penetration, which is the actuator displacement of the testing machine). The rock surface images are provided for one of the small load-drops specified by the red circle as well as the only large load-drop depicted with the blue circle. The rock surface images are taken by the high speed camera (b) before the small load-drop, (c) after the small load-drop, (d) prior to the large load-drop and (e) after the large load-drop. The damaged zones are depicted by dashed boxes.

Figure 6. CT images from the tested specimen of indentation experiment 5. (a) 2D section and (b) 3D view of the indented region. The zone with white color represents removed material and cracks.

Figure 7. (a) Schematic yield surface of the linear Drucker-Prager (D-P) model employed in this study. The pressure (p), which is equal to the negative hydrostatic stress, appears on the horizontal axis and von Mises equivalent stress (q) on the vertical axis. β is the friction angle, and Ψ the dilation angle. (b) Yield surface for the present (D-P) model and the KST model together with the quasi-oedometric test results (Saadati et al. 2018).

Figure 8. (a) Piecewise linear curve fitted with quasi-oedometric test data in order to determine the dilation angle (Ψ). (b) Dilation angle (Ψ) as a function of applied pressure (p).

Figure 9. (a) von Mises equivalent stress-pressure ($q-p$) curve from the finite element (FE) simulation of the quasi-oedometric test. (b) Inelastic axial strain field versus the applied

pressure curves from FE simulations of the quasi-oedometric test for different dilation angles. The experimental results are shown for comparison purposes.

Figure 10. Description of the finite element discretization with **(a)** the geometry including the rock specimen and the rigid indenter, **(b)** a 3D view and **(c)** the top view of the finite element mesh detailing the mesh design in the region (enclosed in dashed box) surrounding the contact zone. A quarter of the rock sample is modeled and the indenter is described by a 3D analytical rigid body.

Figure 11. Force-penetration ($P-h$) curves from FE simulations of the spherical indentation test **(a)** using different material models, and **(b)** additional results for a series of D-P models with tension cut-offs at hydrostatic stresses equal to 10, 20, 30, 40, 50, and 100 MPa.

Figure 12. Stress fields determined from the finite element simulations of the spherical indentation test corresponding to a penetration depth of 0.5 mm. **(a)** Pressure (p) field given by the present model, and **(b)** by the model with zero dilation angle. **(c)** Maximum principal stress field given by the present model, and **(d)** by the model with zero dilation angle. **(e)** Mid principal stress field given by the present model and **(f)** by the model with zero dilation angle. The stresses are expressed in Pa. Note that a negative pressure corresponds to a positive hydrostatic stress.

Figure 13. **(a)** Equivalent plastic strain at the end of loading. **(b)** Tensile normal stress field (along the z -axis shown in Figure 2) determined from the finite element simulation of the spherical indentation test at the end of unloading. The stresses are expressed in Pa.

Figure 14. Force-penetration ($P-h$) curves from finite element simulations of the spherical indentation test with different dilation angles.

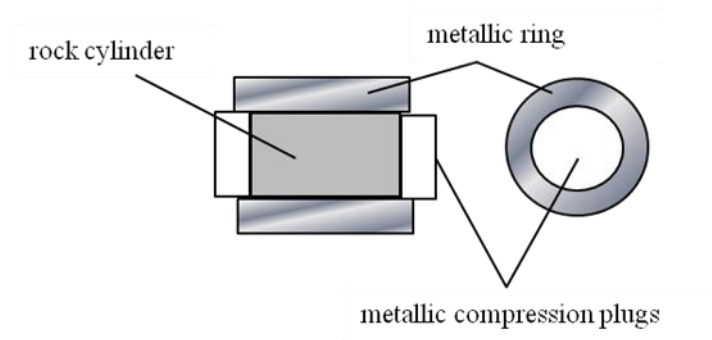


Figure 1

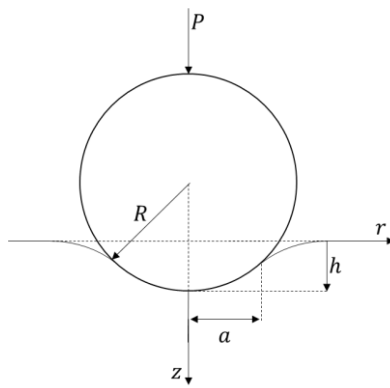


Figure 2

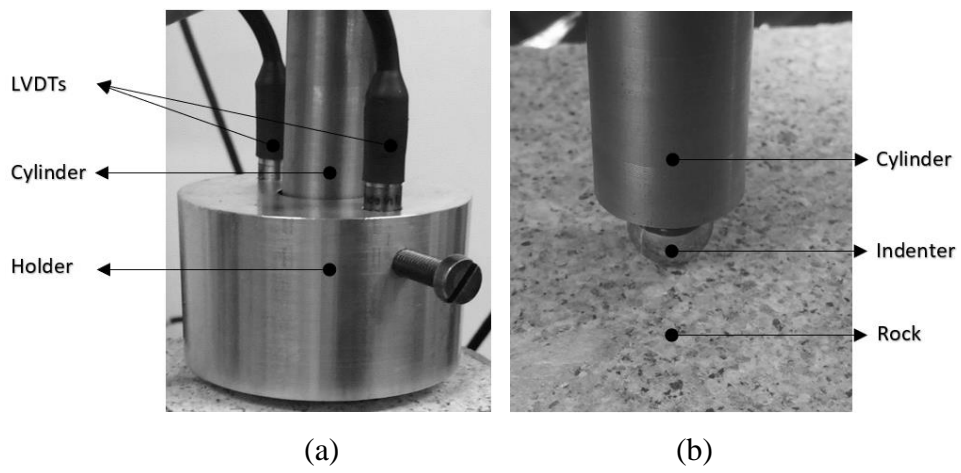


Figure 3

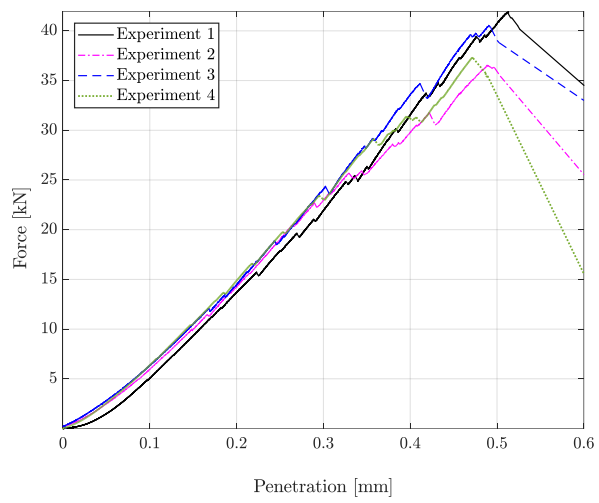
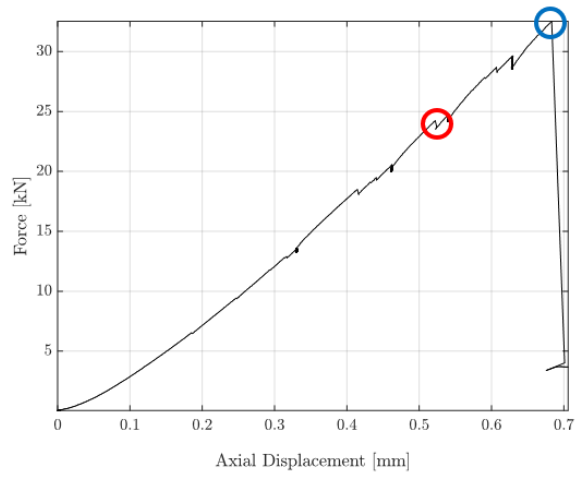
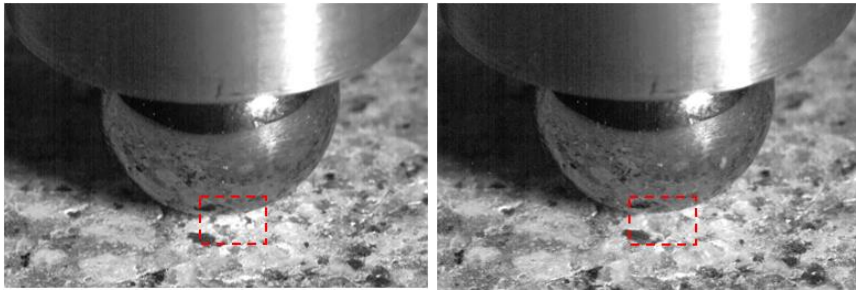


Figure 4

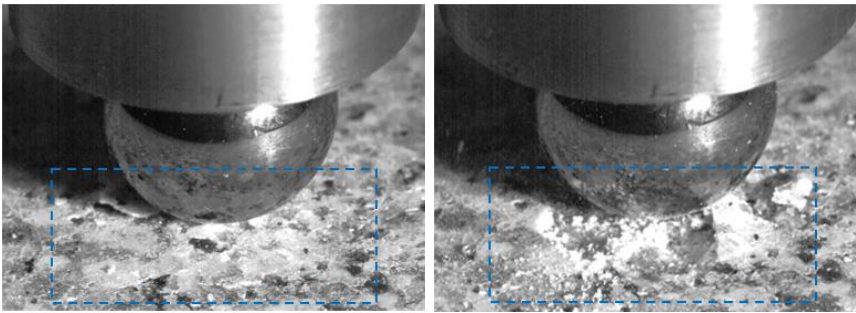


(a)



(b)

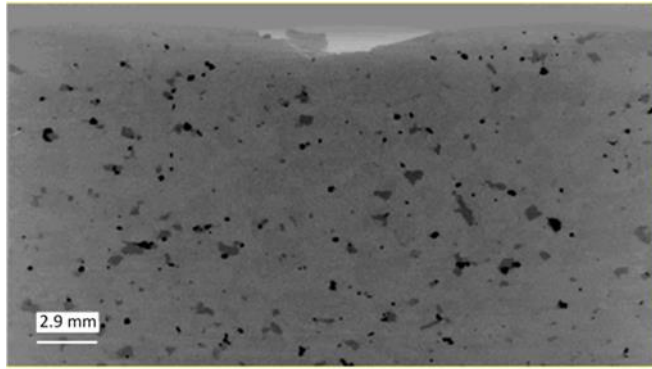
(c)



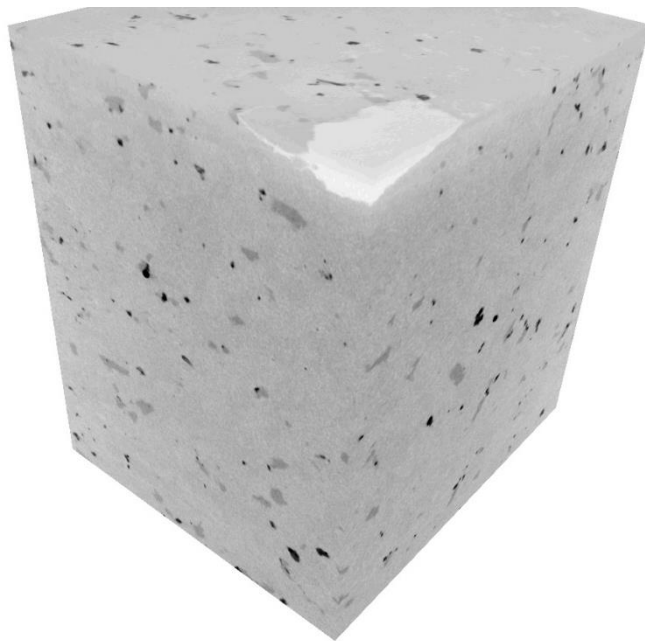
(d)

(e)

Figure 5

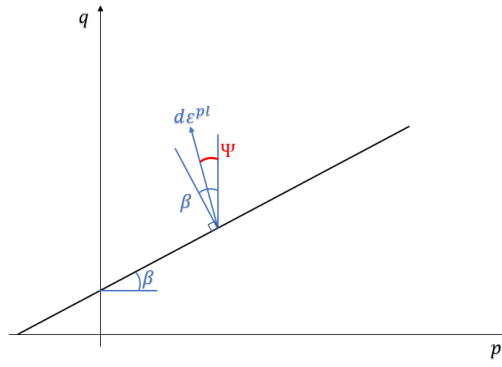


(a)

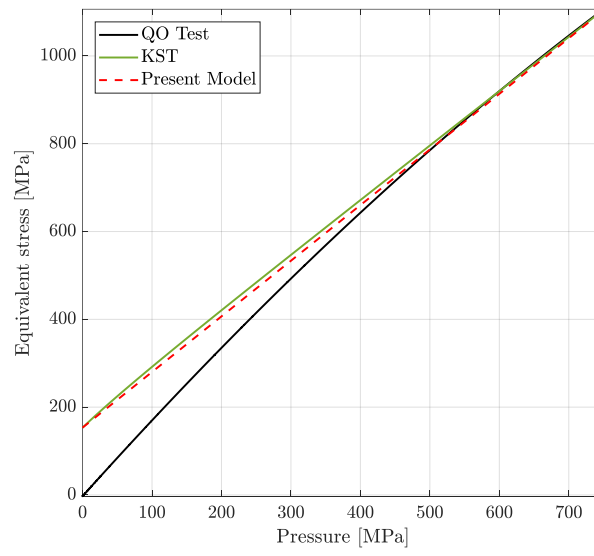


(b)

Figure 6

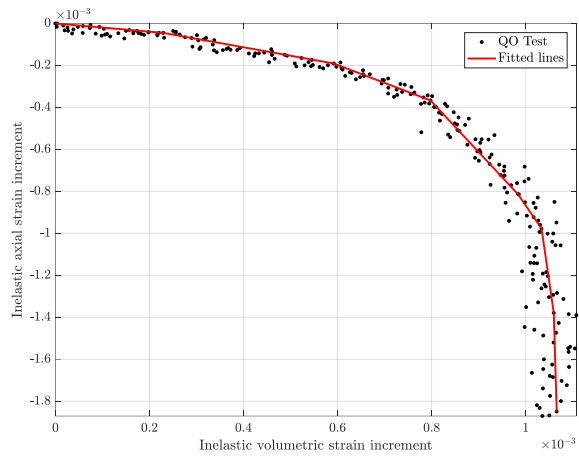


(a)

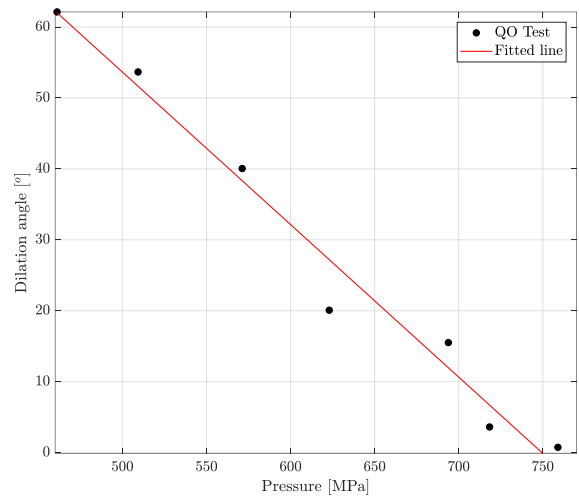


(b)

Figure 7

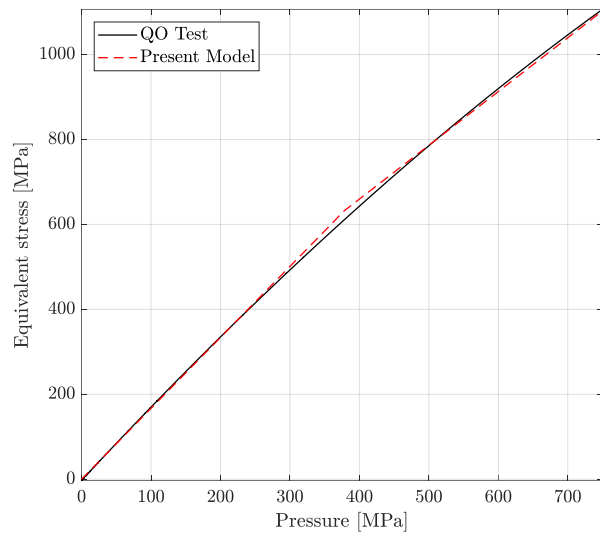


(a)

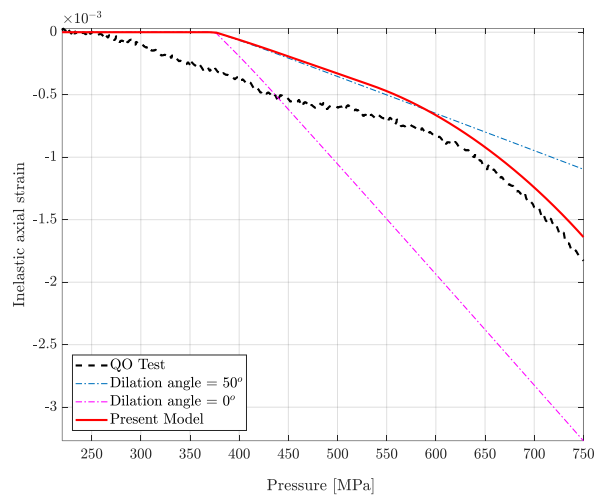


(b)

Figure 8



(a)



(b)

Figure 9

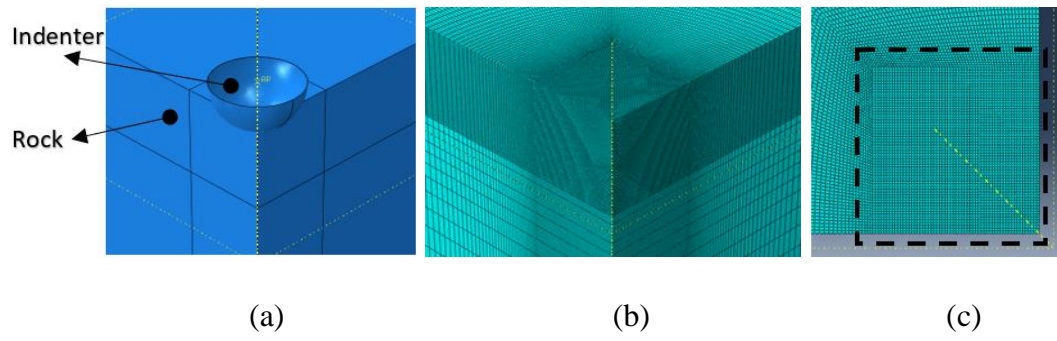
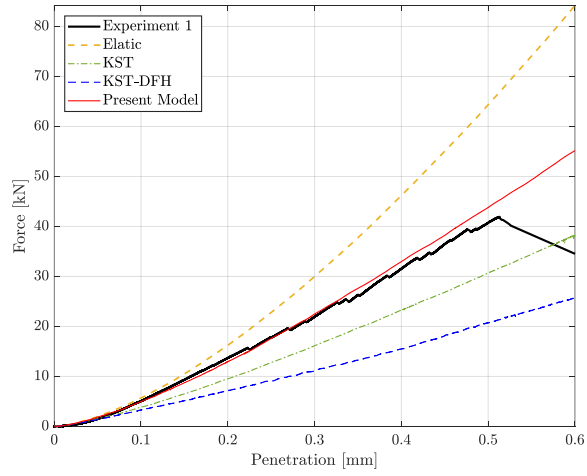
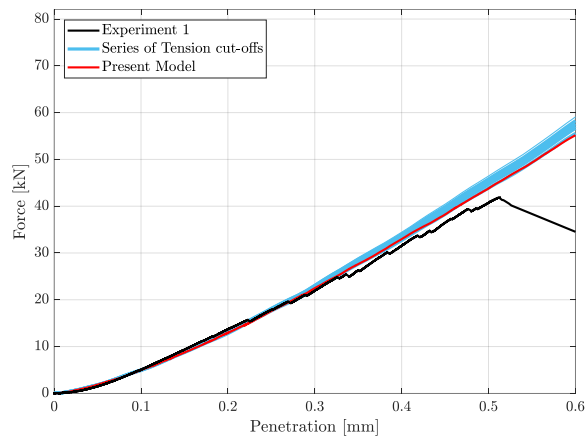


Figure 10



(a)



(b)

Figure 11

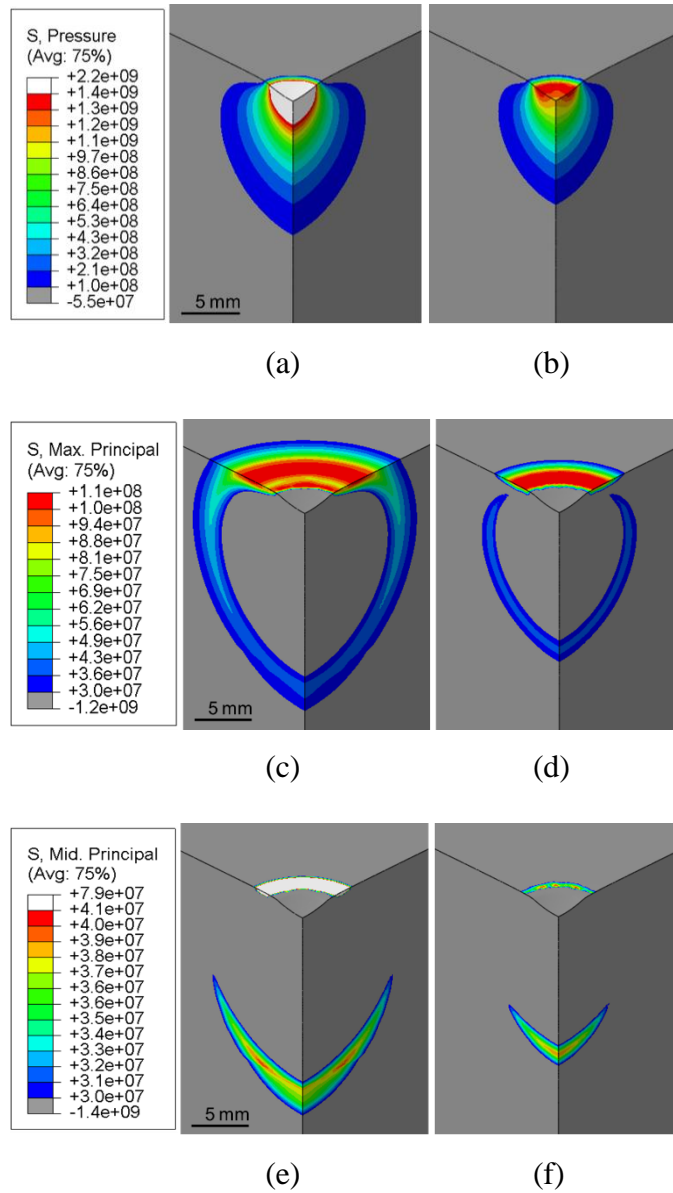
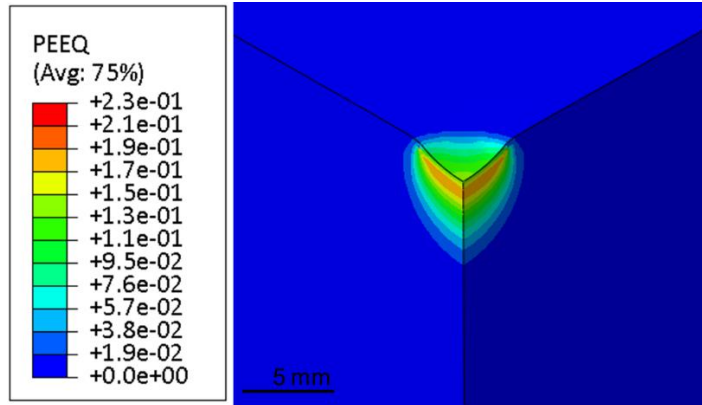
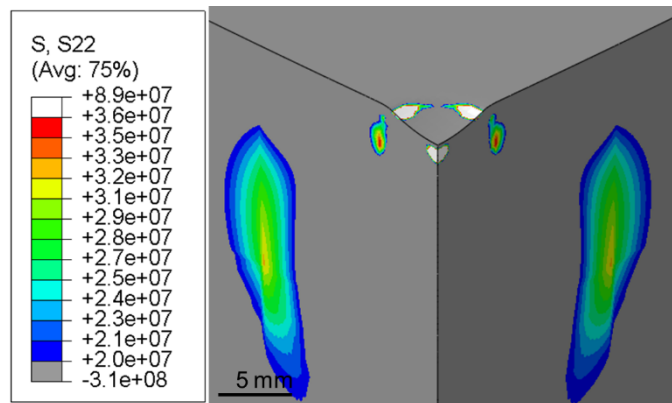


Figure 12



(a)



(b)

Figure 13

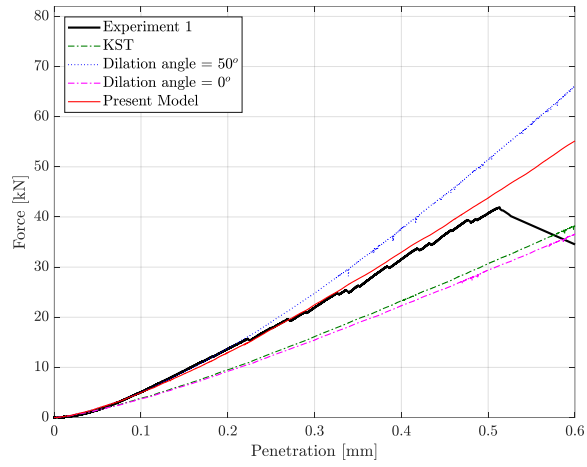


Figure 14